ACS OMEGA

http://pubs.acs.org/journal/acsodf Article

Enhanced Conductivity and Microstructure in Highly Textured $TiN_{1-x}/c\text{-}Al_2O_3$ Thin Films

Alexander Zintler, Robert Eilhardt, Stefan Petzold, Sankaramangalam Ulhas Sharath, Enrico Bruder, Nico Kaiser, Lambert Alff, and Leopoldo Molina-Luna*

Cite This: *ACS Omega* 2022, 7, 2041−2048

Read Online

ACCESS | Metrics & More | Article Recommendations | Supporting Information

ABSTRACT: Titanium nitride thin films are used as an electrode material in superconducting (SC) applications and in oxide electronics. By controlling the defect density in the TiN thin film, the electrical properties of the film can achieve low resistivities and a high critical temperature (T_c) close to bulk values. Generally, low defect densities are achieved by stoichiometric growth and a low grain boundary density. Due to the low lattice mismatch of 0.7%, the best performing TiN layers are grown epitaxially on MgO substrates. Here, we report for the first time a T_c of 4.9 K for ultrathin (23 nm), highly textured (111), and stoichiometric TiN films grown on 8.75% lattice mismatch *c*-cut Al_2O_3 (sapphire) substrates. We demonstrate that with the increasing nitrogen deficiency, the (111) lattice constant increases, which is accompanied by a decrease in T_c. For highly N deficient TiN thin films, no superconductivity could be observed. In addition, a dissociation of grain boundaries (GBs) by the emission of stacking faults could be observed, indicating a combination of two sources for electron scattering defects in the system: (a) volume defects created by nitrogen deficiency and (b) defects created by the presence of GBs. For all samples, the average grain boundary distance is kept constant by a miscut of the *c*-cut sapphire substrate, which allows us to distinguish the effect of nitrogen deficiency and grain boundary density. These properties and surface roughness govern the electrical performance of the films and influence the compatibility as an electrode material in the respective application. This study aims to provide detailed and scale-bridging insights into the structural and microstructural response to nitrogen deficiency in the $c\text{-}Al_2O_3$/TiN system, as it is a promising candidate for applications in state-of-the-art systems such as oxide electronic thin film stacks or SC applications.

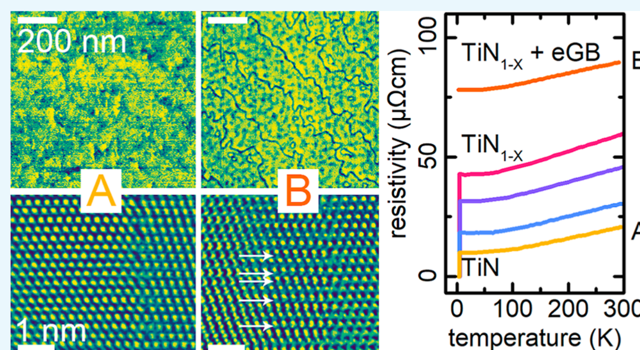

Downloaded via UNIV DARMSTADT on April 28, 2022 at 05:28:25 (UTC).
See https://pubs.acs.org/sharingguidelines for options on how to legitimately share published articles.

1. INTRODUCTION

Titanium nitride (TiN) is an intensely studied electrode material for oxide and superconducting (SC) electronics. For example, the successful combination of TiN and dielectric materials has been demonstrated on hafnium oxide (HfO_2) in complementary metal-oxide-semiconductor field-effect transistors and next-generation Hafnia-based resistive random access memories (RRAM).[1−3] Ferroelectric RAM (FeRAM), which requires symmetric electrodes, can also be realized with TiN as a bottom and top electrode.[4−8] In addition, TiN is a strong candidate as an electrode material in Josephson junctions and SC coplanar waveguides[9] with bulk transition temperature (T_c) of up to 6.0 K[10−12] and exhibits low losses at microwave frequencies.[13] In the search for the highest possible T_c, extensive research including machine learning-based growth parameter prediction is applied.[14] TiN has also gained significant interest in plasmonic and metamaterial applications in the visible and near-infrared wavelength range.[15] The fabrication of TiN electrodes is generally based on thin film deposition by either physical vapor deposition techniques, such as radio frequency (RF) sputtering, chemical vapor deposition (CVD) techniques like inorganic CVD or metal organic CVD (MOCVD), or by sol−gel based approaches.

These films exhibit resistivity values ranging from 14 to 1000 μΩcm for film thicknesses above 40 nm.[9,16−18] Sol−gel based approaches of depositing a TiO_2 film with subsequent nitridation achieved 40 nm TiN films with a 1510 μΩcm resistivity.[19] In most cases, these TiN thin films exhibit a polycrystalline microstructure with a columnar grain growth[20−22] and grain boundaries (GBs) that run along the entire thin film thickness.[23] This microstructure is commonly discussed as the source for reduced conductivity in TiN thin films.[24] The use of highly epitaxial TiN thin films would be

Received: October 4, 2021
Accepted: December 10, 2021
Published: January 3, 2022

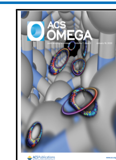

ACS Publications © 2022 The Authors. Published by American Chemical Society

https://doi.org/10.1021/acsomega.1c05505
ACS Omega 2022, 7, 2041−2048

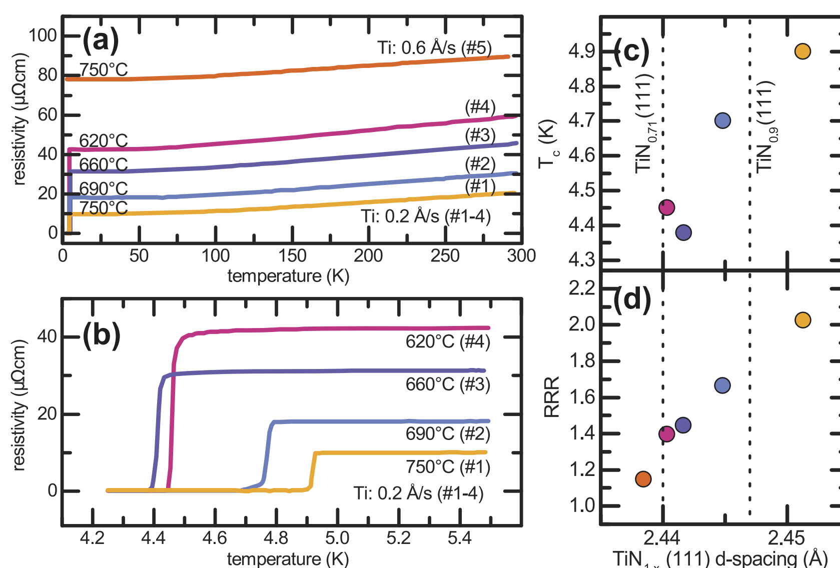

Figure 1. With an increase in growth temperature, the room temperature resistivity ρ(300 K) decreases (a) while T_c increases (b), which is associated with an increase in the residual resistance ratio (RRR = ρ(300 K)/ρ(10 K)), and (c) increase in the TiN_{1-x} (111) *d*-spacing (d); dashed lines indicate literature references for N-deficient and stoichiometric TiN_{1-x} compositions.

advantageous for thin film electronic applications.[25] Epitaxial or single-orientation growth of TiN has been previously reported in the literature using DC reactive sputtering,[26] pulse laser deposition (PLD),[27] atomic layer deposition (ALD),[28,29] and reactive molecular beam epitaxy (RMBE) methods.[9,30] High-quality epitaxy leads to very smooth thin film surfaces and low-defect densities. In the work by Krockenberger et al., TiN grown on MgO substrates by RMBE yields T_c of up to 5.25 K and resistivity in the range of 10−15 $\mu\Omega$cm at 40 nm film thickness.[9] The highest surface quality with a T_c of 5.25 K was obtained for thin films grown at 720 °C. Superconductivity was found to disappear at lower growth temperatures due to a decrease in the nitrogen content of the thin films. As demonstrated by Torgovkin et al., this can be reversed by annealing deficient TiN_{1-x} layers in a nitrogen atmosphere.[12] Chen et al. achieved RMBE-based quasi-epitaxial growth[31] TiN thin films on Si and Al_2O_3 substrates at elevated temperatures, resulting in T_c as high as 5.9 K for 130 nm thick films[30] (closest to bulk TiN, T_c = 6.0 K[11]). At the same time, the presence of nitrogen vacancies and GBs in TiN for RRAM applications has been reported to be beneficial for oxygen incorporation at the HfO_2/TiN interface during resistive switching processes.[32]

To our knowledge, highest surface quality TiN (001) thin films were reported when grown on MgO (001) substrates due to their low lattice mismatch (0.7%). However, Narayan et al. reported the epitaxial growth of TiN (001) on Si(001) substrates by PLD, which was suggested to occur via a domain matching epitaxy.[33] This is unexpected because Si (001) as a substrate for TiN (001) thin films should not yield high epitaxial growth due the high lattice mismatch of 25%. Here, the epitaxy is induced by the common structure, which is composed of four TiN (001) unit cells matching on three Si (001) unit cells, resulting in a lattice mismatch of less than 4%. Reisinger et al. identified a recombination in the Si (001)/TiN (001) system with a "5-on-4-cube-on-cube" reconstruction (lattice mismatch 2.4%) for lower deposition temperatures.[34,35] For 100 nm thick films, Talyansky et al. reported epitaxial growth of TiN (111) film on *c*-cut sapphire substrates with resistivity as low as 13 $\mu\Omega$cm and surface roughness (RMS) of 0.6−1 nm.[36] A high lattice misfit of 8.75% was calculated considering a rhomb-on-rhomb growth on the *c*-cut sapphire substrate.

Although quasi epitaxial growth of TiN thin films was reported for both Silicon and *c*-cut sapphire substrates,[31,37] there is a lack of experimental evidence to clarify the specific nature and properties of the grown microstructures. The high relevance of microstructural effects in TiN is underpinned by studies reporting a total loss of SC for films thinner than 40 nm.[12,16] Most studies are limited by being confined to macroscopic characterization methods like resistivity and X-ray diffraction (XRD) techniques, which allow for functional assessment of the as-grown films, but provide an incomplete picture of the deposited thin films. This study aims at broadening the understanding of defect sources in TiN thin films, namely, nitrogen deficiency and grain boundary density, by combining macroscopic and microscopic investigations down to the atomic level.

2. RESULTS AND DISCUSSION

2.1. TiN_{1-x}—Nitrogen Deficiency. Figure 1a shows the temperature-dependent resistivity measurements of the ~25 nm thick TiN thin films. Films with increasing nitrogen deficiency are presented in the sample series number #1 to #5. The N deficiency was introduced by (a) lowering the substrate temperature and (b) increasing the Ti evaporation rate; see the Experimental Section for further details. Figure 1b shows the low-temperature regime of Figure 1a to reveal the transition temperature to the SC state. Only sample #5 does not show a critical temperature (T_c) above the lowest measurement temperature of 4.2 K. To investigate the influence of the growth temperature in more detail, out-of-plane *d*-spacing (111) values were retrieved from XRD 2θ/ω-scans, as shown in Figure S1. The TiN thin film with the largest *d*-spacing (2.451 Å, #1) shows the highest T_c value (4.9 K), as shown in Figure 1c. T_c drops to 4.4 K at a *d*-spacing of 2.440 Å (#4). The film with the lowest *d*-spacing (2.438 Å, #5) shows no SC. The *d*-spacings found for the different deposition conditions

https://doi.org/10.1021/acsomega.1c05505
ACS Omega 2022, 7, 2041−2048

can be compared to literature data of known stoichiometry, here (111) $TiN_{0.71}$[38] and $TiN_{0.9}$[39] (dashed lines, Figure 1c,d), which allows for the estimation of the nitrogen deficiency. The most stoichiometric film yields a high T_c, whereas the most nitrogen deficient sample shows no T_c. Changing nitrogen deficiency directly translates to the formation of nitrogen vacancies in the crystal lattice.[11] To investigate the defect density of the TiN thin film, the residual resistance ratio (RRR)[12] was calculated (Figure 1d). RRR is defined as the quotient of the resistivity at room temperature (RT) and at 10 K [RRR = ρ(300 K)/ρ(10 K)]. The conductivity at 10 K is an indirect measure of defect density because the (thermal) phonon scattering contribution is greatly reduced at this temperature.[40] In the present system, this defect density is primarily governed by N deficiency shown by a decrease in RRR with smaller d-spacing.

2.2. Thin Film Microstructure. The doubling of resistivity cannot be only explained by the volume defects introduced by the increased nitrogen deficiency. Another source of defects that decreases electrical conductivity in a material is the presence of GBs. A first indication for the presence of GBs would be the existence of more than one in-plane orientation of the (111) oriented TiN grains. The out-of-plane texture that was extracted from the $2\theta/\omega$ scans is TiN (111)||Al_2O_3 (001). The in-plane alignment of the TiN grains can be achieved by azimuthal or ϕ-scan. The results are depicted in Figure S1 and show that TiN {111} peaks are separated by 60° and are offset by ± 30° to the Al_2O_3 {$\bar{1}$02} peaks. This indicates the presence of two in-plane locked crystal orientations or domains, which are 60° in-plane rotated to each other. This was also previously reported for epitaxial TiN (111) thin films on c-cut Al_2O_3 and Si substrates[36,41] where the equivalent TiN (01$\bar{1}$) and (10$\bar{1}$) crystal orientations align along Al_2O_3 (100). The full epitaxial relationship can thus be summarized as follows: TiN (111)|| Al_2O_3 (001) out-of-plane and TiN(01$\bar{1}$),(10$\bar{1}$)||Al_2O_3(100) in-plane.

With an electron mean free path (MFP) of ~100 nm for TiN thin films as estimated by Krockenberger et al.[9] for a 40 nm TiN (001) film on MgO (001), a supposedly grain boundary free TiN film was grown epitaxially on the low lattice mismatch substrate. In the present samples, a grain size distribution analysis provides insights into the contribution of these boundaries in the resistivity.[10] The contribution of these GBs is higher if the distance between the boundaries is the same length scale as the MFP.[42] A common method to image GBs is backscatter electron (BSE) imaging, which has been applied to the present sample series and is displayed in Figure 2.

Figure 2a shows a model for two 60° in-plane rotated TiN grains with GBs indicated by dashed lines. The GBs that are formed can be understood as twins (with boundaries of the ($\bar{1}$2$\bar{1}$)/($\bar{2}$11)/(11$\bar{2}$) type). Figure 2b−f shows representative top-view BSE images of the TiN films. BSE contrast is susceptible to the crystal quality, grain orientation, and RMS. With the film fully aligned in the (111) orientation, the observed contrast should only indicate GBs and roughness. GBs reduce the number of backscattered electrons due to the presence of defects in the crystal lattice, thus giving a detailed view of the thin film microstructure. For the sample with the highest nitrogen deficiency (Figure 2f), GBs are visible as meandering dark lines. For the samples grown at 620, 660, and 690 °C and the stoichiometric sample grown at 750 °C, no distinct GBs can be observed. Dark spots observed for the low

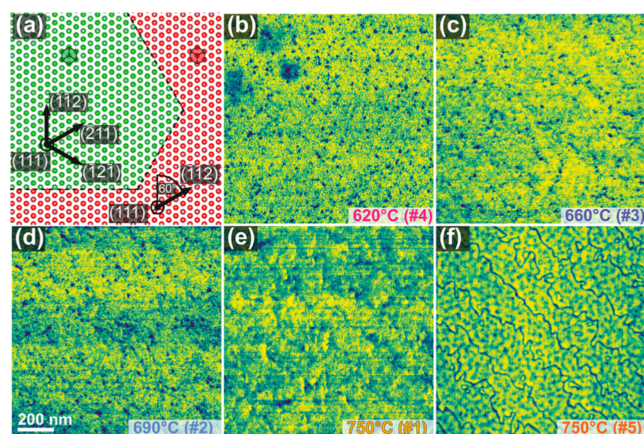

Figure 2. (a) Twin grain boundary of two 60° in-plane rotated TiN grains (red and green). (b−e) Top view BSE maps of the SC TiN thin films showing no visible GBs in contrast to the non-SC TiN thin film (f). False color is applied to enhance contrast.

growth temperature samples (Figure 2b−d) can be correlated with the increase in RMS as indicated by the X-ray reflectometry (XRR) results (Figure S3a) down to a RMS of 1.5 nm for the films grown at 750 °C. The meandering of the boundaries in the sample shown in Figure 2f does not indicate a random behavior, but it follows a set of three dominating orientations. They correspond to the twin boundaries marked by dashed lines shown in Figure 2a. Consequently, this indicates the presence of a high number of twin boundaries for the sample shown in Figure 2f.

With BSE imaging, no GBs could be observed for the samples grown at lower temperatures. However, XRD ϕ-scans indicate that there are two orientations of the TiN grains present in each sample. To investigate the microstructure of all samples, ion channeling contrast (iCC) imaging[43] was performed, as shown in Figure 3. The imaging conditions were selected to give the strongest iCC between the two orientations. A sample tilt of 54° from the 30 keV Ga ion beam allowed the ions to penetrate one TiN orientation at the prominent (001) zone axis, while the other grain orientation would be oriented at the same time along the ($\bar{1}$22) zone axis. The discrepancy between the index of the zone axis directly correlates with the secondary electron (SE) yield and thus the observed contrast in the images (prominent {001} zone axis, low SE yield; {$\bar{1}$22} zone axis, high SE yield).[44] With the high contrast achieved in an otherwise featureless surface, this method proved to be ideal to identify grain sizes and microstructures in this system, which can also be optimized by a ϕ/azimuth rotation series. In the iCC images, large, over 100 nm sized grains can be observed for all samples.

The anisotropy of the grain size can be attributed to a miscut of the c-cut sapphire substrate, which was used for all samples. Cuccureddu et al. found that even for nominally 0° miscut "c-cut" samples, there are still surface steps present that are homogeneously distributed on the surface.[45] For a 0.15° miscut c-Al_2O_3 sample, the step width was found to be 120 nm. In addition, annealing leads to a "bunching" of the surface steps if they are held at elevated temperatures, meaning that each resulting step height is a multiple of $c/6$ = 2.2 Å of the Al_2O_3 c-axis unit cell parameter (c = 13 Å). The step width and height converge to uniformity.[46] The (111) d-spacing value of TiN is 2.439 Å, which is a ~10% deviation of the $c/6$ Al_2O_3 = 2.2 Å (see Figure S4) lattice constant along growth direction. A

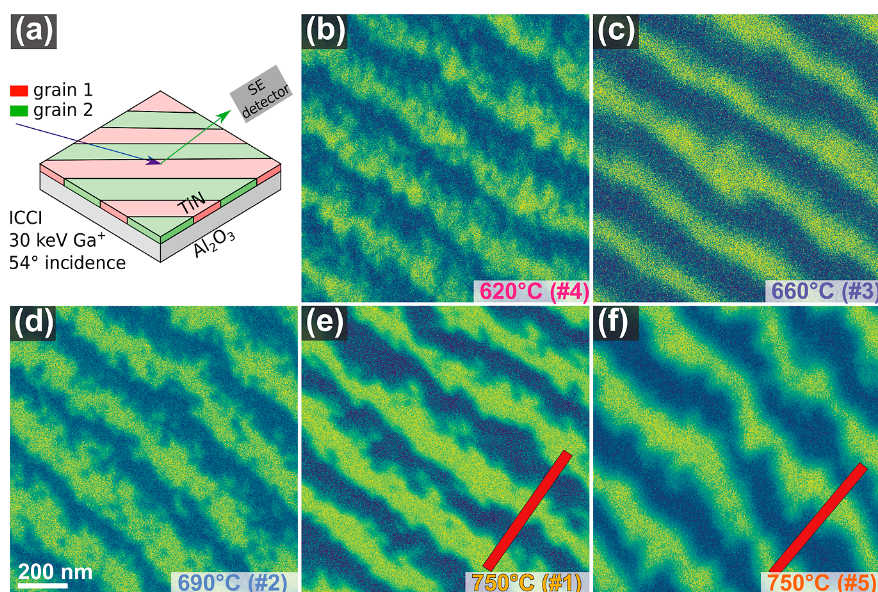

Figure 3. (a) Ion channeling contrast (iCC) imaging geometry. (b−f) iCC images of the samples revealing an elongated grain structure with comparable grain sizes for all samples. Red lines (e,f) showing the orientation of the cross sections cut in the subsequent focused ion beam lamella preparation, perpendicular to the observed GBs.

bunched surface step of $5*c/6$ Al_2O_3 would introduce an overall mismatch of 56%, whereas a surface step of $9*c/6$ Al_2O_3 would be a full TiN (111) *d*-spacing. Depending on the step height, the bonding configuration for the first adatom differ[47] and might trigger the respective TiN in-plane rotation (the out-of-plane direction fixed by the rhomb-on-rhomb epitaxy). By this high degree of ordering, the observed consistent alternation of in-plane orientations can be understood as an effect of uniform step widths and heights on the seeding conditions. The investigated TiN films have been grown on the same batch of substrates, which were heated during deposition and which will therefore yield to similar surface steps, as indicated by the uniform grain size distribution throughout the sample series. The four-point electrode geometry used in the resistivity measurement was not aligned with the observed elongation. The anisotropy, induced by the substrate miscut, dictates one crucial source for defects in the thin film: the grain boundary density. It is virtually the same for all samples and thus will have the same contribution for all samples. For the following high-resolution scanning transmission electron microscopy (HR-STEM) analysis, cross-sectional FIB lamellae have been cut from the samples grown at 750 °C. Cutting was performed perpendicular to the elongated grain structures (indicated in Figure 3e,f) to ensure that the GBs are aligned along the observation direction of the STEM.

2.3. Atomic Structure of (Dissociated) Twin GBs.

Figure 4 shows representative cross sections of GBs for the samples grown at 750 °C. The sets of neighboring grains are all oriented with (111) pointing upward along growth direction, which confirms the observations of the $2\theta/\omega$ scans (Figure 1). Both of the imaged GBs can be indexed as twin boundaries of the $\{\bar{1}2\bar{1}\}$ type. For the sample grown at a Ti evaporation rate of 0.2 Å/s (Figure 4a), atomic resolution high-angle annular dark-field (HAADF)-STEM imaging shows that the defects present at the boundary are located at the boundary itself, where the joining of the lattices of the grains form periodic recombination sites along the boundary. This is in stark

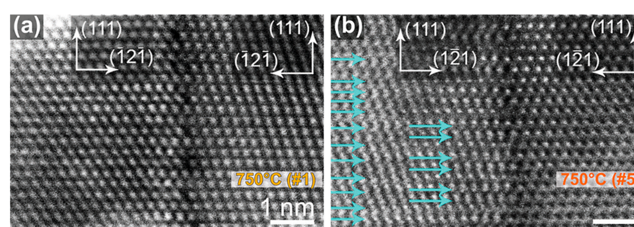

Figure 4. High-angle annular dark-field scanning transmission electron microscopy (HAADF-STEM) images of $\{\bar{1}2\bar{1}\}$ twin boundaries in the (a) SC and (b) non-SC TiN thin films. The grain boundary in (b) shows a high density of stacking faults in the atomic resolution image, indicated by blue arrows.

contrast to the boundary of the sample grown at 0.6 Å/s (Figure 4b). Here, an extended defect structure indicated by split atomic columns (indicated by blue arrows) can be observed. These variations in contrast can be attributed to stacking faults along the (111) axis for the left grain shown in Figure 4b. Twin boundary dissociation by stacking fault emission is observed for other systems[48,49] as well as for TiN, but up until this point, only under mechanical deformation.[50] Strain induced by the lattice mismatch in the present substrate/thin film stack in combination with the growth conditions of the RMBE deposition process was reported as the cause for the occurrence of stacking faults in the Si/GaAs system.[51,52] Here, the volume affected by stacking faults extends through the full film thickness up to the surface of the film, where it gives rise to the grain boundary contrast found in the BSE images (Figure 2f), as they pose a sample volume of high defect concentration, reducing the backscatter yield.

Strongly confined geometrical conditions for the microstructure developed during the thin film growth process have a direct impact on the physical properties. A high fraction of high symmetry boundaries are generally associated with reduced resistance in conductors.[41,53] This is the case in our study because the microstructure of the TiN films contains almost solely twin boundaries. If the average grain size is in the

https://doi.org/10.1021/acsomega.1c05505
ACS Omega 2022, 7, 2041−2048

range of the MFP, the grain boundary can be considered as a main contributor to electron scattering, increasing the resistivity.[24,54] Due to the equal average grain size in the present sample series, the impact on resistivity should therefore be equivalent. Nonetheless, the defects associated with the extended GBs play a crucial role in the contribution to the resistivity. Extended scattering regions lead to higher resistivity, which is described as a reduction of "grain boundary transparency" in terms of electrical conduction across a grain boundary.[55−57] This is directly evident in the increase of conductivity (Figure 1a). There is also a higher concentration of oxygen[12] and other contaminants[58] expected at the boundaries, which could negatively affect electronic transport properties.

In their application as bottom electrodes for valence change memory RRAM devices, the ability of the electrodes to incorporate oxygen plays a fundamental role in the resistive switching process.[59−63] Nitrogen-deficient TiN thin films lower the energy necessary to incorporate oxygen ions in the electrode material.[32] As GBs form a localized high density of defects, especially for the dissociated GBs observed in this work, they would have the potential to locally facilitate electroforming and switching processes.[3] As the microstructure of the TiN electrode also defines the growth conditions—or conditions for crystallization by annealing for ALD grown films[64]—GBs present a predefined seeding location and thus will have a direct influence on the microstructure observed in subsequent layers of a thin film stack.[3] This influence can be further addressed by nanoscale orientation mapping techniques like automated crystal orientation mapping in a plan-view geometry.[65]

3. CONCLUSIONS

The impact of nitrogen deficiency on the room and low temperature conductivity as well as on the microstructure and type of evolving GBs was studied for the c-Al_2O_3/TiN system. By combining XRD $2\theta/\omega$, ϕ-scans, BSE, iCC imaging in a multibeam FIB system and atomic resolution HR-STEM, the microstructure, grain size, and type of GBs were determined. The ~25 nm thick TiN films exhibit a homogeneous (111) out-of-plane texture, with a set of two in-plane rotations, separated by 60°. This texture is defined by the quasi epitaxial growth of (111) TiN on c-Al_2O_3 where the large lattice mismatch of 8.75% is compensated by a rhomb-on-rhomb configuration. A fixed grain size as observed for the present sample series allowed us to separate the grain boundary density, as one contributor to defect density, from the effect of increasing nitrogen deficiency. The observed grain boundary density and the anisotropy of the grain size are directly related to the surface step density found on nominally 0° c-cut sapphire substrates. These steps also define the initial seeding conditions of the TiN grains and result in the alternating in-plane rotations observed in the thin film microstructure. Increased nitrogen deficiency has three effects on the film properties: (a) the loss of superconductivity, (b) an increase in resistivity, and (c) grain boundary dissociation by stacking fault emission. Nonetheless, the same morphological quality is achieved. Stoichiometric, ultrathin 25 nm films are achieved for the first time with a room-temperature conductivity of 10 $\mu\Omega$cm and a T_c of 4.9 K with a RMS of ~1.5 nm. The observed properties match best in class SC epitaxially grown TiN films on MgO substrates.

4. EXPERIMENTAL SECTION

BSE imaging was performed on a Tescan Mira3 XMH at 15 kV, 320 μs dwell time and 434 pA specimen current using a Deben 4 quadrant detector. Ion beam channeling contrast (iCC) imaging and cross-sectional focused ion beam (FIB) sample preparation for scanning transmission electron microscopy (STEM) were performed on a JEOL JIB-4600F, and iCC imaging was conducted at 30 keV acceleration voltage. Atomic resolution high-angle annular dark-field (HAADF) STEM imaging was performed on a JEOL JEM-ARM200F operated at 200 kV with a semiconvergence angle of 25 mrad.

In this study, an electron-beam evaporation setup was used to evaporate elemental sources of titanium (99.99%, Chempur). Nitrogen radicals obtained using a RF plasma source (Oxford Applied Research, HD25) were used as the source of nitridation in our experiments. Mass flow controllers (MFC) allowed us to control the flow rates of nitrogen (99.995% purity) to the radical sources. The growth temperature was increased from 620 to 750 °C with a constant Ti evaporation rate of 0.2 Å/s, a nitrogen flow of 1.0 sccm, and a RF power of 200 W. For a sample with higher nitrogen deficiency, a Ti evaporation rate of 0.6 Å/s has been selected. Initial selection of the growth parameters included aspects like minimization of nitrogen deficiency[26] stoichiometry, RMS, and grain size.[17,66]

XRD and XRR were performed on a Rigaku (SmartLab) X-ray diffractometer by using Cu Kα_1 (λ = 1.54057 Å) at 45/170 kV/mA and a parallel beam geometry and on a Seifert PTS by using Cu K$\alpha_{1,2}$ (λ = 1.54057 Å) at 40/40 kV/mA and a parallel beam geometry with a graphite monochromator.

A Keithley 6221 model current source and Keithley 2182A model nanovoltmeter were used for the presented four-probe resistivity measurements, while the temperature was measured using a calibrated Lakeshore silicon diode sensor (model DT-670D-SD), placed in contact with the sample stage.

■ ASSOCIATED CONTENT

Supporting Information

The Supporting Information is available free of charge at https://pubs.acs.org/doi/10.1021/acsomega.1c05505.

XRD 2θ scans for all samples, indicating the TiN (111) lattice parameter change due to nitrogen deficiency; XRD ϕ scans for all samples of TiN {111} and Al_2O_3 (102), showing the in-plane alignment of the film to substrate; XRR scans for all samples, indicating RMS and film density; and VESTA[67] models of the substrate and film, indicating the (001)/6 Al_2O_3 and (111) TiN lattice spacings (PDF)

■ AUTHOR INFORMATION

Corresponding Author

Leopoldo Molina-Luna − *Advanced Electron Microscopy, Institute of Materials Science, TU Darmstadt, 64287 Darmstadt, Germany;* orcid.org/0000-0002-9412-8093; Phone: +49 6151 16 20180; Email: leopoldo.molina-luna@aem.tu-darmstadt.de, molina@aem.tu-darmstadt.de

Authors

Alexander Zintler − *Advanced Electron Microscopy, Institute of Materials Science, TU Darmstadt, 64287 Darmstadt, Germany;* orcid.org/0000-0002-2272-3184

https://doi.org/10.1021/acsomega.1c05505
ACS Omega 2022, 7, 2041−2048

Robert Eilhardt − *Advanced Electron Microscopy, Institute of Materials Science, TU Darmstadt, 64287 Darmstadt, Germany*
Stefan Petzold − *Advanced Thin Film Technology, Institute of Materials Science, TU Darmstadt, 64287 Darmstadt, Germany*
Sankaramangalam Ulhas Sharath − *Advanced Thin Film Technology, Institute of Materials Science, TU Darmstadt, 64287 Darmstadt, Germany*
Enrico Bruder − *Physical Metallurgy, Institute of Materials Science, TU Darmstadt, 64287 Darmstadt, Germany*
Nico Kaiser − *Advanced Thin Film Technology, Institute of Materials Science, TU Darmstadt, 64287 Darmstadt, Germany;* orcid.org/0000-0002-5644-890X
Lambert Alff − *Advanced Thin Film Technology, Institute of Materials Science, TU Darmstadt, 64287 Darmstadt, Germany*

Complete contact information is available at:
https://pubs.acs.org/10.1021/acsomega.1c05505

Notes

The authors declare no competing financial interest.

■ ACKNOWLEDGMENTS

This work was supported by the European Research Council (ERC) "Horizon 2020" Program under Grant no. 805359-FOXON and the Deutsche Forschungsgemeinschaft (DFG) under project 384682067 and was undertaken in the framework of the WAKeMeUP and StorAIge projects, which has received funding from the Electronic Components and Systems for European Leadership Joint Undertaking in collaboration with the European Union's H2020 Framework Programme (Grant no. H2020/2014−2020) and National Authorities, under Grant Agreement nos. 3783176 and 101007321 as well by the Federal Ministry of Education and Research (BMBF) under contract 16MEE0154. The authors thank Dr. Joachim Brötz for assisting with the $2\theta/\omega$ and ϕ XRD scans. We acknowledge support by the Deutsche Forschungsgemeinschaft (DFG − German Research Foundation) and the Open Access Publishing Fund of Technische Universität Darmstadt.

■ REFERENCES

(1) Sharath, S. U.; Vogel, S.; Molina-Luna, L.; Hildebrandt, E.; Wenger, C.; Kurian, J.; Duerrschnabel, M.; Niermann, T.; Niu, G.; Calka, P.; Lehmann, M.; Kleebe, H.-J.; Schroeder, T.; Alff, L. Control of Switching Modes and Conductance Quantization in Oxygen Engineered HfOxbased Memristive Devices. *Adv. Funct. Mater.* **2017**, *27*, 1700432.
(2) Waser, R.; Dittmann, R.; Staikov, G.; Szot, K. Redox-Based Resistive Switching Memories - Nanoionic Mechanisms, Prospects, and Challenges. *Adv. Mater.* **2009**, *21*, 2632−2663.
(3) Petzold, S.; Zintler, A.; Eilhardt, R.; Piros, E.; Kaiser, N.; Sharath, S. U.; Vogel, T.; Major, M.; McKenna, K. P.; Molina-Luna, L.; Alff, L. Forming-Free Grain Boundary Engineered Hafnium Oxide Resistive Random Access Memory Devices. *Adv. Electron. Mater.* **2019**, *5*, 1900484.
(4) Böscke, T. S.; Müller, J.; Bräuhaus, D.; Schröder, U.; Böttger, U. Ferroelectricity in Hafnium Oxide Thin Films. *Appl. Phys. Lett.* **2011**, *99*, 102903.
(5) Hyuk Park, M.; Joon Kim, H.; Jin Kim, Y.; Lee, W.; Moon, T.; Seong Hwang, C. Evolution of Phases and Ferroelectric Properties of Thin Hf0.5Zr0.5O2 Films According to the Thickness and Annealing Temperature. *Appl. Phys. Lett.* **2013**, *102*, 242905.
(6) Cao, R.; Wang, Y.; Zhao, S.; Yang, Y.; Zhao, X.; Wang, W.; Zhang, X.; Lv, H.; Liu, Q.; Liu, M. Effects of Capping Electrode on Ferroelectric Properties of Hf0.5Zr0.5O2 Thin Films. *IEEE Electron Device Lett* **2018**, *39*, 1207.
(7) Schroeder, U.; Richter, C.; Park, M. H.; Schenk, T.; Pešić, M.; Hoffmann, M.; Fengler, F. P. G.; Pohl, D.; Rellinghaus, B.; Zhou, C.; Chung, C.-C.; Jones, J. L.; Mikolajick, T. Lanthanum-Doped Hafnium Oxide: A Robust Ferroelectric Material. *Inorg. Chem.* **2018**, *57*, 2752−2765.
(8) Max, B.; Hoffmann, M.; Mulaosmanovic, H.; Slesazeck, S.; Mikolajick, T. Hafnia-Based Double-Layer Ferroelectric Tunnel Junctions as Artificial Synapses for Neuromorphic Computing. *ACS Appl. Electron. Mater.* **2020**, *2*, 4023−4033.
(9) Krockenberger, Y.; Karimoto, S.-i.; Yamamoto, H.; Semba, K. Coherent Growth of Superconducting TiN Thin Films by Plasma Enhanced Molecular Beam Epitaxy. *J. Appl. Phys.* **2012**, *112*, 083920.
(10) Ningthoujam, R. S.; Gajbhiye, N. S. Synthesis, electron transport properties of transition metal nitrides and applications. *Prog. Mater. Sci.* **2015**, *70*, 50−154.
(11) Spengler, W.; Kaiser, R.; Christensen, A. N.; Müller-Vogt, G. Raman Scattering, Superconductivity, and Phonon Density of States of Stoichiometric and Nonstoichiometric TiN. *Phys. Rev. B: Solid State* **1978**, *17*, 1095−1101.
(12) Torgovkin, A.; Chaudhuri, S.; Ruhtinas, A.; Lahtinen, M.; Sajavaara, T.; Maasilta, I. J. High Quality Superconducting Titanium Nitride Thin Film Growth Using Infrared Pulsed Laser Deposition. *Supercond. Sci. Technol.* **2018**, *31*, 055017.
(13) Vissers, M. R.; Gao, J.; Wisbey, D. S.; Hite, D. A.; Tsuei, C. C.; Corcoles, A. D.; Steffen, M.; Pappas, D. P. Low Loss Superconducting Titanium Nitride Coplanar Waveguide Resonators. *Appl. Phys. Lett.* **2010**, *97*, 232509.
(14) Ohkubo, I.; Hou, Z.; Lee, J. N.; Aizawa, T.; Lippmaa, M.; Chikyow, T.; Tsuda, K.; Mori, T. Realization of Closed-Loop Optimization of Epitaxial Titanium Nitride Thin-Film Growth via Machine Learning. *Mater. Today Phys.* **2021**, *16*, 100296.
(15) Naik, G. V.; Saha, B.; Liu, J.; Saber, S. M.; Stach, E. A.; Irudayaraj, J. M. K.; Sands, T. D.; Shalaev, V. M.; Boltasseva, A. Epitaxial Superlattices with Titanium Nitride as a Plasmonic Component for Optical Hyperbolic Metamaterials. *Proc. Natl. Acad. Sci. U.S.A.* **2014**, *111*, 7546−7551.
(16) Xiang, W.; Liu, Y.; Zhang, J. Influence of Microstructure on the Electrical Properties of Heteroepitaxial TiN Films. *Electron. Mater. Lett.* **2018**, *14*, 314−318.
(17) Savvides, N.; Window, B. Electrical Transport, Optical Properties, and Structure of TiN Films Synthesized by Low-energy Ion Assisted Deposition. *J. Appl. Phys.* **1988**, *64*, 225−234.
(18) Sun, N.; Zhou, D.; Liu, W.; Shi, S.; Tian, Z.; Liu, F.; Li, S.; Wang, J.; Ali, F. Tailoring Surface Chemistry and Morphology of Titanium Nitride Electrode for On-Chip Supercapacitors. *ACS Sustainable Chem. Eng.* **2020**, *8*, 7869−7878.
(19) Valour, A.; Higuita, M. A. U.; Guillonneau, G.; Crespo-Monteiro, N.; Jamon, D.; Hochedel, M.; Michalon, J.-Y.; Reynaud, S.; Vocanson, F.; Jiménez, C.; Langlet, M.; Donnet, C.; Jourlin, Y. Optical, Electrical and Mechanical Properties of TiN Thin Film Obtained from a TiO2 Sol-Gel Coating and Rapid Thermal Nitridation. *Surf. Coat. Technol.* **2021**, *413*, 127089.
(20) Yu, J.; Phang, P.; Samundsett, C.; Basnet, R.; Neupan, G. P.; Yang, X.; Macdonald, D. H.; Wan, Y.; Yan, D.; Ye, J. Titanium Nitride Electron-Conductive Contact for Silicon Solar Cells By Radio Frequency Sputtering from a TiN Target. *ACS Appl. Mater. Interfaces* **2020**, *12*, 26177−26183.
(21) Grosso, S.; Latu-Romain, L.; Berthomé, G.; Renou, G.; Le Coz, T.; Mantel, M. Titanium and Titanium Nitride Thin Films Grown by Dc Reactive Magnetron Sputtering Physical Vapor Deposition in a Continuous Mode on Stainless Steel Wires: Chemical, Morphological and Structural Investigations. *Surf. Coat. Technol.* **2017**, *324*, 318−327.
(22) Sun, N.; Zhou, D.; Shi, S.; Liu, W.; Zhao, X.; Liu, F.; Tian, Z.; Li, S.; Wang, J.; Ali, F. DC Substrate Bias Enables Preparation of

Superior-Performance TiN Electrode Films over a Wide Process Window. *Mater. Res. Bull.* **2019**, *119*, 110575.
(23) Xu, Z.; Zhang, Z.; Bartosik, M.; Zhang, Y.; Mayrhofer, P. H.; He, Y. Insight into the Structural Evolution during TiN Film Growth via Atomic Resolution TEM. *J. Alloys Compd.* **2018**, *754*, 257−267.
(24) Patsalas, P.; Logothetidis, S. Optical, Electronic, and Transport Properties of Nanocrystalline Titanium Nitride Thin Films. *J. Appl. Phys.* **2001**, *90*, 4725−4734.
(25) Grossi, A.; Walczyk, D.; Zambelli, C.; Miranda, E.; Olivo, P.; Stikanov, V.; Feriani, A.; Sune, J.; Schoof, G.; Kraemer, R.; Tillack, B.; Fox, A.; Schroeder, T.; Wenger, C.; Walczyk, C. Impact of Intercell and Intracell Variability on Forming and Switching Parameters in RRAM Arrays. *IEEE Trans. Electron Devices* **2015**, *62*, 2502−2509.
(26) Johansson, B. O.; Sundgren, J. E.; Greene, J. E.; Rockett, A.; Barnett, S. A. Growth and Properties of Single Crystal TiN Films Deposited by Reactive Magnetron Sputtering. *J. Vac. Sci. Technol., A* **1985**, *3*, 303−307.
(27) Bonholzer, M.; Lorenz, M.; Grundmann, M. Layer-by-Layer Growth of TiN by Pulsed Laser Deposition on in-Situ Annealed (100) MgO Substrates. *Phys. Status Solidi A* **2014**, *211*, 2621−2624.
(28) Elers, K.-E.; Winkler, J.; Weeks, K.; Marcus, S. TiCl4 as a Precursor in the TiN Deposition by ALD and PEALD. *J. Electrochem. Soc.* **2005**, *152*, G589.
(29) Kim, J.; Hong, H.; Ghosh, S.; Oh, K.-Y.; Lee, C. Physical Properties of Highly Conformal TiN Thin Films Grown by Atomic Layer Deposition. *Jpn. J. Appl. Phys.* **2003**, *42*, 1375.
(30) Olson, G. A. Growth of Titanium-Nitride Thin Films for Low-Loss Superconducting Quantum Circuits. Ph.D. Thesis, University of Illinois at Urbana-Champaign, 2015. http://hdl.handle.net/2142/87951.
(31) Chen, W.-C.; Lin, Y.-R.; Guo, X.-J.; Wu, S.-T. Heteroepitaxial TiN of Very Low Mosaic Spread on Al2O3. *Jpn. J. Appl. Phys.* **2003**, *42*, 208.
(32) Bradley, S. R.; McKenna, K. P.; Shluger, A. L. The Behaviour of Oxygen at Metal Electrodes in HfO2 Based Resistive Switching Devices. *Microelectron. Eng.* **2013**, *109*, 346−350.
(33) Narayan, J.; Tiwari, P.; Chen, X.; Singh, J.; Chowdhury, R.; Zheleva, T. Epitaxial Growth of TiN Films on (100) Silicon Substrates by Laser Physical Vapor Deposition. *Appl. Phys. Lett.* **1992**, *61*, 1290−1292.
(34) Reisinger, D.; Schonecke, M.; Brenninger, T.; Opel, M.; Erb, A.; Alff, L.; Gross, R. Epitaxy of Fe3O4 on Si(001) by Pulsed Laser Deposition Using a TiN/MgO Buffer Layer. *J. Appl. Phys.* **2003**, *94*, 1857−1863.
(35) Willmott, P. R.; Timm, R.; Huber, J. R. RHEED Analysis of Interface Growth Modes of TiN Films on Si(001) Produced by Crossed Beam Laser Ablation. *Appl. Surf. Sci.* **1998**, *127−129*, 105−110.
(36) Talyansky, V.; Choopun, S.; Downes, M. J.; Sharma, R. P.; Venkatesan, T.; Li, Y. X.; Salamanca-Riba, L. G.; Wood, M. C.; Lareau, R. T.; Jones, K. A. Pulsed Laser Deposition of Titanium Nitride Films on Sapphire. *J. Mater. Res.* **1999**, *14*, 3298−3302.
(37) Volz, K.; Stolz, W.; Dadgar, A.; Krost, A. Growth of III/Vs on Silicon. In *Handbook of Crystal Growth*; Kuech, T. F., Ed., 2nd ed.; North-Holland: Boston, 2015; pp 1249−1300.
(38) Holmberg, B.; Yhland, M.; Dahlbom, R.; Sjövall, J.; Theander, O.; Flood, H. Structural Studies on the Titanium-Nitrogen System. *Acta Chem. Scand.* **1962**, *16*, 1255−1261.
(39) Christensen, A. N.; Hämäläinen, R.; Turpeinen, U.; Andresen, A. F.; Smidsrød, O.; Pontchour, C.-O.; Phavanantha, P.; Pramatus, S.; Cyvin, B. N.; Cyvin, S. J. The Temperature Factor Parameters of Some Transition Metal Carbides and Nitrides by Single Crystal X-Ray and Neutron Diffraction. *Acta Chem. Scand.* **1978**, *32a*, 89−90.
(40) Wilson, A. H. The Second Order Electrical Effects in Metals. *Math. Proc. Cambridge Philos. Soc.* **1937**, *33*, 371−379.
(41) Hultman, L.; Ljungcrantz, H.; Hallin, C.; Janzén, E.; Sundgren, J.-E.; Pécz, B.; Wallenberg, L. R. Growth and Electronic Properties of Epitaxial TiN Thin Films on 3C-SiC(001) and 6H-SiC(0001) Substrates by Reactive Magnetron Sputtering. *J. Mater. Res.* **1996**, *11*, 2458−2462.
(42) Zhu, Y. F.; Lang, X. Y.; Zheng, W. T.; Jiang, Q. Electron Scattering and Electrical Conductance in Polycrystalline Metallic Films and Wires: Impact of Grain Boundary Scattering Related to Melting Point. *ACS Nano* **2010**, *4*, 3781−3788.
(43) Giannuzzi, L. A.; Michael, J. R. Comparison of Channeling Contrast between Ion and Electron Images. *Microsc. Microanal.* **2013**, *19*, 344−349.
(44) Silk, J. R.; Dashwood, R. J.; Chater, R. J. Determination of Lattice Orientation in Aluminium Alloy Grains by Low Energy Gallium Ion-Channelling. *Nucl. Instrum. Methods Phys. Res., Sect. B* **2010**, *268*, 2064−2068.
(45) Cuccureddu, F.; Murphy, S.; Shvets, I. V.; Porcu, M.; Zandbergen, H. W.; Sidorov, N. S.; Bozhko, S. I. Surface Morphology of C-Plane Sapphire (α-Alumina) Produced by High Temperature Anneal. *Surf. Sci.* **2010**, *604*, 1294−1299.
(46) Gossmann, H. J.; Sinden, F. W.; Feldman, L. C. Evolution of Terrace Size Distributions during Thin-film Growth by Step-mediated Epitaxy. *J. Appl. Phys.* **1990**, *67*, 745−752.
(47) Lee, H.-J.; Fujii, K.; Goto, T.; Yao, T.; Chang, J. Effects of Controlled Ambidirectional Nucleation on the Heteroepitaxial Growth of M-GaN on m-Sapphire. *Appl. Phys. Lett.* **2011**, *98*, 071904.
(48) Lucadamo, G.; Medlin, D. L. Geometric Origin of Hexagonal Close Packing at a Grain Boundary in Gold. *Science* **2003**, *300*, 1272−1275.
(49) Rittner, J. D.; Seidman, D. N.; Merkle, K. L. Grain-Boundary Dissociation by the Emission of Stacking Faults. *Phys. Rev. B: Condens. Matter Mater. Phys.* **1996**, *53*, R4241−R4244.
(50) Zhang, L.; Wu, Y.; Yu, W.; Shen, S. Response of symmetric tilt grain boundary in titanium nitride under shear. *Eng. Anal. Bound. Elem.* **2019**, *105*, 231−241.
(51) Giannini, C.; Carlino, E.; Sciacovelli, P.; Tapfer, L.; Sauvage-Simkin, M.; Garreau, Y.; Jedrecy, N.; Véron, M. B.; Pinchaux, R. Influence of the Interface Layer on the Strain Relaxation of ZnSe Epitaxial Layers Grown by MBE on (001)GaAs. *J. Phys. D: Appl. Phys.* **1999**, *32*, A51−A55.
(52) Kim, S.-D.; Harris, J. S. Stacking Fault Stability in GaAs/Si Hetero-Epitaxial Growth. *J. Cryst. Growth* **1992**, *123*, 439−444.
(53) Lu, L.; Shen, Y.; Chen, X.; Qian, L.; Lu, K. Ultrahigh Strength and High Electrical Conductivity in Copper. *Science* **2004**, *304*, 422−426.
(54) Kasap, S.; Koughia, C.; Ruda, H. E. Electrical Conduction in Metals and Semiconductors. In *Springer Handbook of Electronic and Photonic Materials*; Kasap, S., Capper, P., Eds.; Springer International Publishing: Cham, 2017; p 1.
(55) Reiss, G.; Vancea, J.; Hoffmann, H. Grain-Boundary Resistance in Polycrystalline Metals. *Phys. Rev. Lett.* **1986**, *56*, 2100−2103.
(56) Olaya, J. J.; Huerta, L.; Rodil, S. E.; Escamilla, R. Superconducting Niobium Nitride Films Deposited by Unbalanced Magnetron Sputtering. *Thin Solid Films* **2008**, *516*, 8768−8773.
(57) Bishara, H.; Lee, S.; Brink, T.; Ghidelli, M.; Dehm, G. Understanding Grain Boundary Electrical Resistivity in Cu: The Effect of Boundary Structure. *ACS Nano* **2021**, *15*, 16607−16615.
(58) Ohya, S.; Chiaro, B.; Megrant, A.; Neill, C.; Barends, R.; Chen, Y.; Kelly, J.; Low, D.; Mutus, J.; O'Malley, P. J. J.; Roushan, P.; Sank, D.; Vainsencher, A.; Wenner, J.; White, T. C.; Yin, Y.; Schultz, B. D.; Palmstrøm, C. J.; Mazin, B. A.; Cleland, A. N.; Martinis, J. M. Room Temperature Deposition of Sputtered TiN Films for Superconducting Coplanar Waveguide Resonators. *Supercond. Sci. Technol.* **2013**, *27*, 015009.
(59) Gutiérrez Moreno, J. J.; Nolan, M. Ab Initio Study of the Atomic Level Structure of the Rutile TiO2(110)−Titanium Nitride (TiN) Interface. *ACS Appl. Mater. Interfaces* **2017**, *9*, 38089−38100.
(60) McKenna, K. P. Structure, Electronic Properties, and Oxygen Incorporation/Diffusion Characteristics of the Σ 5 TiN(310)[001] Tilt Grain Boundary. *J. Appl. Phys.* **2018**, *123*, 075301.
(61) Niu, G.; Calka, P.; Huang, P.; Sharath, S. U.; Petzold, S.; Gloskovskii, A.; Fröhlich, K.; Zhao, Y.; Kang, J.; Schubert, M. A.;

Bärwolf, F.; Ren, W.; Ye, Z.-G.; Perez, E.; Wenger, C.; Alff, L.; Schroeder, T. Operando Diagnostic Detection of Interfacial Oxygen 'Breathing' of Resistive Random Access Memory by Bulk-Sensitive Hard X-Ray Photoelectron Spectroscopy. *Mater. Res. Lett.* **2019**, *7*, 117−123.

(62) Yong, Z.; Persson, K.-M.; Saketh Ram, M.; D'Acunto, G.; Liu, Y.; Benter, S.; Pan, J.; Li, Z.; Borg, M.; Mikkelsen, A.; Wernersson, L.-E.; Timm, R. Tuning Oxygen Vacancies and Resistive Switching Properties in Ultra-Thin HfO2 RRAM via TiN Bottom Electrode and Interface Engineering. *Appl. Surf. Sci.* **2021**, *551*, 149386.

(63) Starschich, S.; Menzel, S.; Böttger, U. Evidence for Oxygen Vacancies Movement during Wake-up in Ferroelectric Hafnium Oxide. *Appl. Phys. Lett.* **2016**, *108*, 032903.

(64) Eilhardt, R.; Zintler, A.; Recalde, O.; Nasiou, D.; Petzold, S.; Alff, L.; Molina-Luna, L. Birth of a Grain Boundary: In Situ TEM Observation of the Microstructure Evolution in HfO2 Based Memristors. *Microsc. Microanal.* **2021**, *27*, 1238−1239.

(65) Zintler, A.; Eilhardt, R.; Wang, S.; Krajnak, M.; Schramowski, P.; Stammer, W.; Petzold, S.; Kaiser, N.; Kersting, K.; Alff, L.; Molina-Luna, L. Machine Learning Assisted Pattern Matching: Insight into Oxide Electronic Device Performance by Phase Determination in 4D-STEM Datasets. *Microsc. Microanal.* **2020**, *26*, 1908−1909.

(66) Chowdhury, R.; Vispute, R. D.; Jagannadham, K.; Narayan, J. Characteristics of Titanium Nitride Films Grown by Pulsed Laser Deposition. *J. Mater. Res.* **1996**, *11*, 1458−1469.

(67) Momma, K.; Izumi, F. VESTA 3 for Three-Dimensional Visualization of Crystal, Volumetric and Morphology Data. *J. Appl. Crystallogr.* **2011**, *44*, 1272−1276.